J. Fluid Mech. (2001), *vol.* 427, *pp.* 329–358. Printed in the United Kingdom

Experimental and computational study of laminar cavity flows at hypersonic speeds

By A. P. JACKSON, R. HILLIER AND S. SOLTANI†

Department of Aeronautics, Imperial College of Science, Technology and Medicine, London, SW7 2BY, UK

(Received 3 February 2000 and in revised form 22 August 2000)

This paper presents a combined experimental/computational study of a surface cavity in a low Reynolds number Mach 9 flow. The geometry is based on a body of revolution, which produces highly two-dimensional time-averaged flow for all experimental test cases. A range of cavity length-to-depth ratios, up to a maximum of 8, is investigated. These correspond to 'closed' cavity flows, with the free shear layer bridging the entire cavity. For most cases the free shear layer is laminar. However, there is evidence of three-dimensional unsteadiness which is believed to be the consequence of Taylor–Görtler-type vortex formation. The effect of this is first detected on the cavity floor but progressively spreads as the cavity length is increased. For the longest cavities the flow is also influenced by the early stages of laminar–turbulent transition in the free shear layer.

1. Introduction

In high-speed aerodynamics there is a distinct advantage to developing a close integration between experiment and computational fluid dynamics. Measurement of many flow field quantities is difficult or impossible, and model manufacture is expensive and time-consuming. Thus CFD can assist in configuration design and can also be used to 'probe' areas and flow field properties that are not accessible to experimental measurement. In turn, the ideal experiment should be intended not only to investigate the flow physics but should also be a suitable test problem to support code development and evaluation. Increasingly, therefore, experiments need to be designed as 'benchmark' studies, with careful attention to data quality. The present investigation is one of several in the area of flow separation at hypersonic speeds, in which we attempt to approach the study in this spirit.

A rectangular cavity was selected as the test configuration, both because of its practical relevance and also because of various experimental and computational advantages. In particular: the separation position is more-or-less fixed by geometry; the cavity length can be changed easily to vary flow characteristics; a simple Cartesian mesh is one potential option for the computational grid. In attempting to define the experimental data precisely two main criteria were used in the model design: the mean flow should be two-dimensional to the highest standards possible and (more difficult) the cavity flow should be laminar. The intention is to provide precise conditions for the numerical study, without the complexity of flow three-dimensionality or the uncertainties of turbulence modelling. Later papers will consider both turbulent, and three-dimensional, cavity flows.

† Present address: Renault, Mecanique des Fluides et Combustion, France.

Cavity flows are of considerable importance at hypersonic speeds and feature in small-scale detail, such as surface defects, pitting and gaps in joints and between insulation tiles, and also in larger-scale features such as fuel injection slots and gaps between body surfaces and control surfaces. More generally, cavity flows have been studied over a very wide range of Mach numbers. From subsonic up to moderate supersonic speeds they are often characterized by very strong unsteadiness and resonance phenomena (for example Rossiter 1966; Rockwell & Naudascher 1978; Merzkirch, Page & Fletcher 1988; Zhang 1995), particularly when the cavity scale is large compared with the thickness of the approach boundary layer. Flow unsteadiness has also been reported for hypersonic separations generally (see for example Dolling & Murphy 1983 and Erengil & Dolling 1991 for ramp-induced separations) and for cavity flows in particular (Unalmis, Clemens & Dolling 1998 and Morgenstern & Chokani 1994). The conditions for the onset of unsteadiness are not clear, however, and hypersonic separations do not usually experience the same large-scale shedding of vorticity found at lower speeds. Many cases are effectively steady, especially so if the flow is laminar, which is the specific regime of interest here.

Kinetic heating is particularly important at hypersonic speeds and is, in fact, the main focus of interest in our experiments – partly because of its practical relevance but also because it is a (relatively) easily measured quantity which is a sensitive test for CFD predictions. Early studies showed that the overall convective heat flux, through the wetted surface of a cavity, is less than that for an equivalent length of attached boundary layer flow. For the case of a very thin boundary layer at separation, and ignoring the cavity vortex system, Chapman (1956) used control volume arguments to predict an upper limit of order 50% for laminar flows, which has been borne out reasonably well by subsequent experiments. In further studies the effect of the initial boundary layer on the development of the laminar free shear layer was considered by, amongst others, Denison & Baum (1963), Kubota & Dewey (1964) and Charwat & Der (1966). Large development distances are required to reach an asymptotic profile, so that in many practical problems the shear layer is likely to be in an early state of non-self-similar growth. High localized heating rates, very substantially more than those for the equivalent attached boundary layer, are found at shear layer impingement on the back face of the cavity. Chung & Viegas (1961) modelled an impinging shear layer as incompressible, rotational and inviscid, the 'surface' values on the back face of the cavity providing edge conditions for the growth of the laminar wall boundary layer. This was subsequently modified by Nestler (1970) and Hodgson (1970) to approximate the effects of compressibility and of a finite initial boundary layer thickness at separation. These papers identify the almost singular nature of the heating at the reattachment lip and its rapid fall with distance from the lip. For most flows the characteristic length scale for this fall is so small that accurate measurement of the extreme heating rates close to the reattachment lip is difficult.

These theories cannot provide general information on the cavity flow, in particular the effect of the cavity vortex systems, which can only be resolved by detailed experiment or computation. Most experiments have been conducted on planar configurations. Such data are *nominally* two-dimensional, therefore, but may be influenced by three-dimensional effects (particularly in separated flow studies) introduced by sidewall (or lack of sidewall) constraints. For this reason a body of revolution has been used in the present study. This still does not guarantee, of course, that the resultant flow will itself be two-dimensional (axisymmetric), but any departures from axisymmetry will be a feature of the basic flow physics. The axisymmetric downstream-facing step of Roshko & Thomke (1966), for example, shows secondary or cellular

M_∞	$P0_\infty$ (bar)	$T0_\infty$ (K)	T_{wall} (K)	Re_∞ (m^{-1})
8.9 ($\pm$0.5%)	98 ($\pm$2%)	1000 ($\pm$4%)	293 ($\pm$2%)	9 540 000 ($\pm$6%)

TABLE 1. Test section flow conditions.

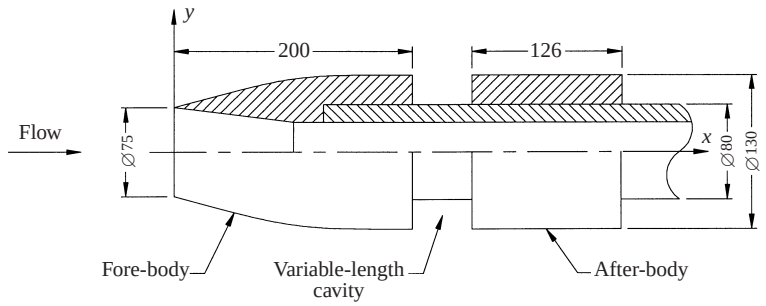

FIGURE 1. Schematic of the hollow test model. All dimensions are in mm. The cavity depth D is 25 mm. The cavity length, L, is variable up to 250 mm.

flows on the body surface, both upstream and downstream of reattachment. Other hypersonic studies which have based a cavity flow on an axisymmetric configuration include those of Hahn (1969) and Nicholl (1964).

2. Test facility and experimental techniques

The experimental work was carried out in the Gun Tunnel of the Aeronautics Department of Imperial College. This is a short-test-time facility, operating with nitrogen gas, with a total flow duration of 20 ms and a test window of about 4–8 ms. Test conditions for this study are given in table 1.

Model static pressures were measured with Kulite XCQ-093 miniature transducers. These were positioned in the model skin, with the sensing head 2.5 mm below the surface, and connected to the model surface by a 0.5 mm diameter tapping. This provided a frequency response of 10 kHz. A static calibration of the transducers was carried out before each run and the final data accuracy is approximately $\pm$ 4%. Surface heat transfer rates were measured by the thin-film technique, using platinum resistance thermometers, hand-painted and baked onto a machinable ceramic substrate, MACOR. The temperature histories were reduced to heat transfer rates using the algorithm due to Cook & Felderman (1966), also described in Schultz & Jones (1973). Data were low-pass filtered at 4 kHz, with an expected final accuracy of about $\pm$ 8%. Spatial resolution of the gauges was 5 mm circumferentially, effectively 5° in azimuth, and 0.25 mm for axial or radial distributions. Near separation and reattachment extremely large surface gradients were developed. The data recorded by a gauge are essentially the average over the gauge area and the final data are plotted at the gauge centre. All heat transfer data (q) are presented in W cm^{-2}.

3. Model design criteria

The test model is the hollow body of revolution shown in figure 1. The fore-body has a chord length of 200 mm. For $0.0 \leqslant x \leqslant 34.7444$ the outer profile is a straight

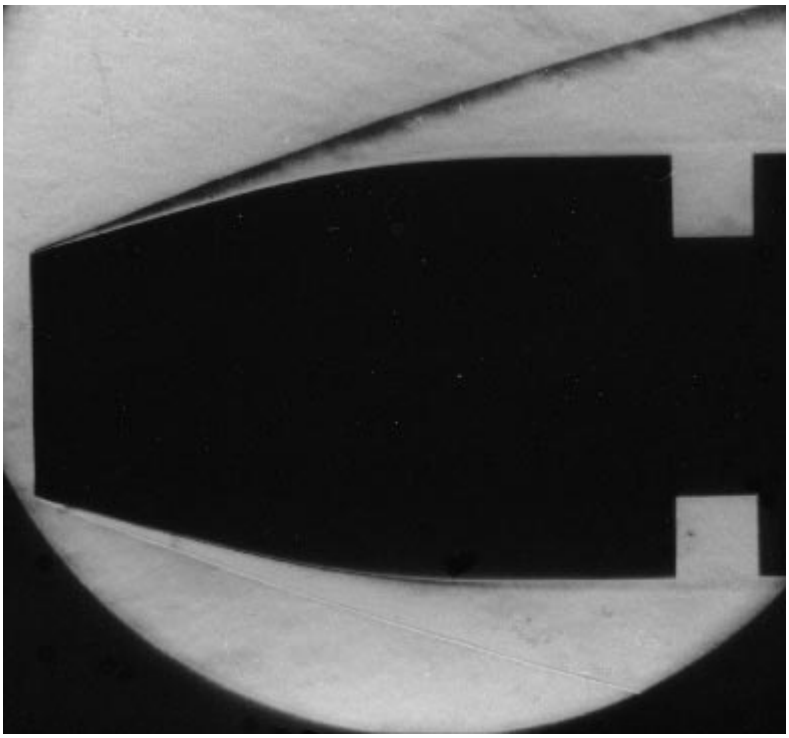

FIGURE 2. $L/D = 1$. Flow field schlieren.

x	r	x	r	x	r
40.1976	48.2693	90.2032	59.9621	140.1744	64.6875
50.0213	50.8668	100.2366	61.5664	150.3334	64.8975
60.4147	53.5159	110.3213	62.8108	159.9298	64.9805
70.2969	55.8806	120.4421	63.7120	170.0911	64.9998
80.2242	58.0479	130.0208	64.2969		

TABLE 2. Coordinates for model fore-body. Chord length, x, and radius, r, are both in mm.

line with $r(\text{mm}) = 37.5 + 0.267949x$. For $172.913 \leqslant x \leqslant 200.0$ the outer profile is a cylinder, with the same radius as the after-body, of $r = 65.0$. A high-order curve was fitted between these two plane portions. A sample set of coordinates is listed in table 2.

The after-body can be moved axially along the central support, providing variations in the cavity length, L, up to a maximum of 10 cavity depths, D. The general configuration evolved from the two main test requirements discussed in § 1. To produce axisymmetric flow required considerable care in model manufacture, and careful alignment of the model at zero incidence during experiment, but the high quality of axisymmetry actually achieved will be apparent in the following sections. The second requirement was to produce laminar cavity flow. The precise criteria to achieve this are not known, but clearly a 'sufficiently low' model Reynolds number is required. This has to be achieved through a combination of low test-flow unit Reynolds number and small model size, which provides a conflict between the need

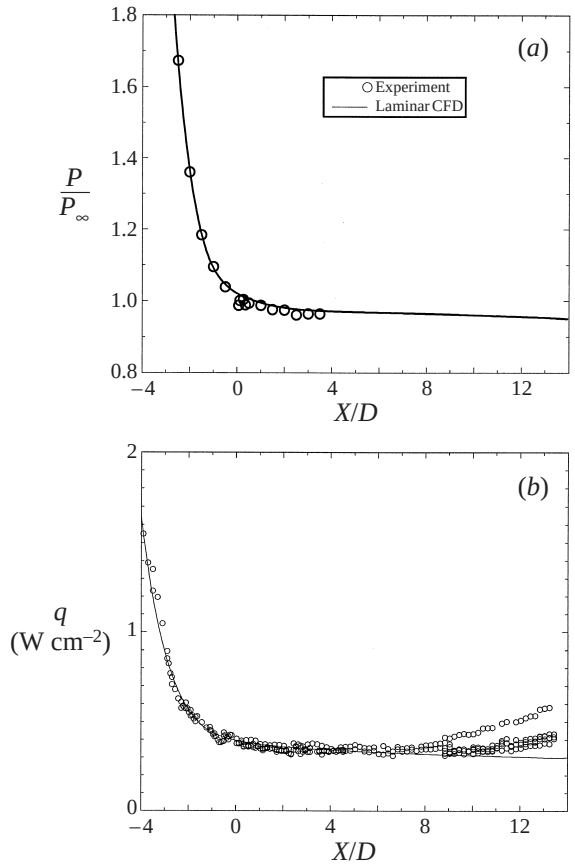

FIGURE 3. No-cavity case: (*a*) surface pressure, (*b*) surface heat transfer. The intended separation position is located at $X/D = 0$.

for measurable levels of heat transfer and for good spatial resolution of the data. Aided by preliminary computations, a cavity depth of 25 mm was chosen as the minimum to resolve as much as possible of the very steep flow gradients expected near the reattachment lip. The unit Reynolds number given in table 1 is the lowest feasible operating value for the tunnel but tests by Mallinson *et al.* (1997*b*) showed that it should be sufficient to maintain laminar *attached* boundary layer flow up to a chord length of at least 400 mm. Knowledge of compressible free shear layer transition is incomplete, but various hypersonic cavity studies (for example Chapman, Kuehn & Larson 1958; Nicholl 1964; Larson & Keating 1960) have all suggested that the separated shear layer for a surface cavity is 'as stable as the corresponding attached laminar boundary layer'. The fore-body length prior to the cavity was therefore fixed at 200 mm, and data presented in the next section will show that the free shear layer remains laminar up to cavity L/D values of about 6 or 7.

The hollow body shown in figure 1 was the best way to reconcile the need for a body of revolution with the required cavity depth and the restriction on the fore-body length. As an additional constraint the internal duct must 'swallow' the transient wave system generated during tunnel starting, otherwise the interior flow chokes and a detached shock wave system forms at the model inlet. The upper limit on the ratio of inlet radius to the interior duct radius was determined by experiment and

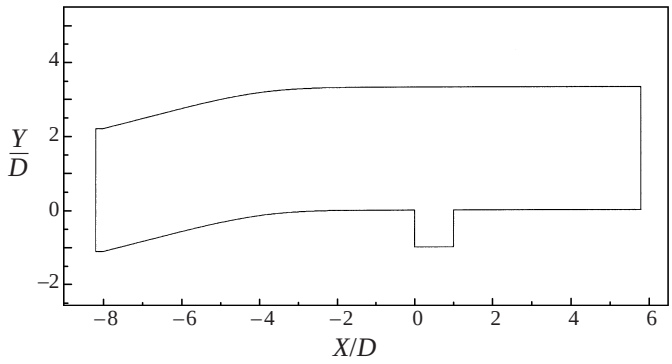

FIGURE 4. Computational domain for the cavity and the region external to the body of revolution.

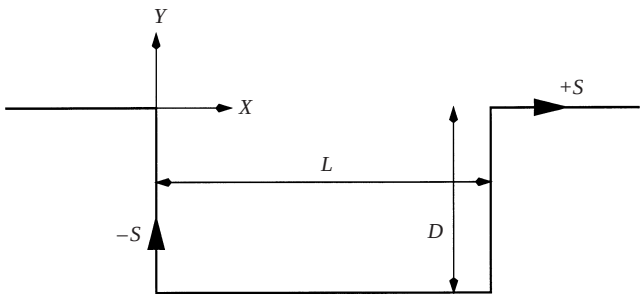

FIGURE 5. Schematic of coordinate system for the cavity.

all test data correspond to an attached leading-edge shock wave system as shown in figure 2. The resulting inlet diameter of 75 mm is less than the required outer diameter of 130 mm, so that a profiled fore-body was necessary. This was developed, computationally, so as to provide a monotonic fall in the surface pressure from the leading edge up to the intended separation position (at 200 mm from the leading edge) and as close as possible to zero axial pressure gradient further downstream. The detail of the final shape is given in Appendix A and the resultant measured pressure distribution together with the CFD, for the 'no-cavity' body, is shown in figure 3. Here the axial distance X is referenced to zero at the intended position for the cavity leading edge and is also normalized by the intended cavity depth D. The general configuration is similar to one used by Hahn (1969) for a cavity flow study at Mach 7.3.

4. Computational modelling

The flow solver (Hillier, Kirk & Soltani 1995) employs a 'time-splitting' technique, on a structured mesh, whereby inviscid fluxes are calculated using a second-order upwind Godunov-type method and viscous fluxes are evaluated using centred differencing, giving overall second-order accuracy in space and time. The computations assume axisymmetric, laminar flows, using a Prandtl number of 0.72 and the viscosity–temperature formulation for nitrogen due to Keyes (1952).

The basic computational domain for the shortest cavity case ($L/D = 1$) is shown in figure 4 and a schematic of the coordinate system in figure 5. Here axial and

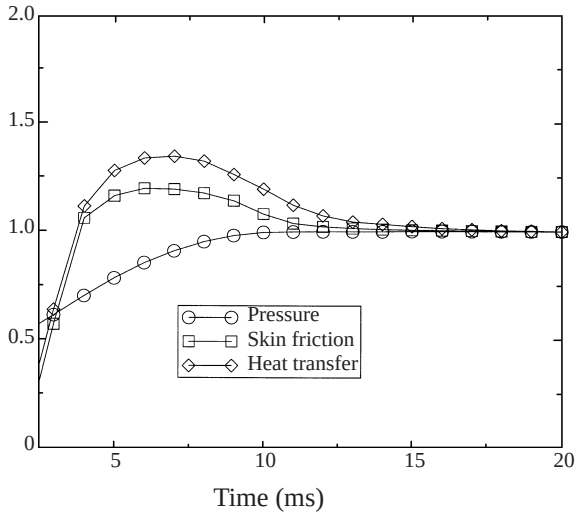

FIGURE 6. Cavity $L/D = 1$. Computational modelling of the development, with time, of flow properties on the cavity floor. Data are normalized by their steady-state values.

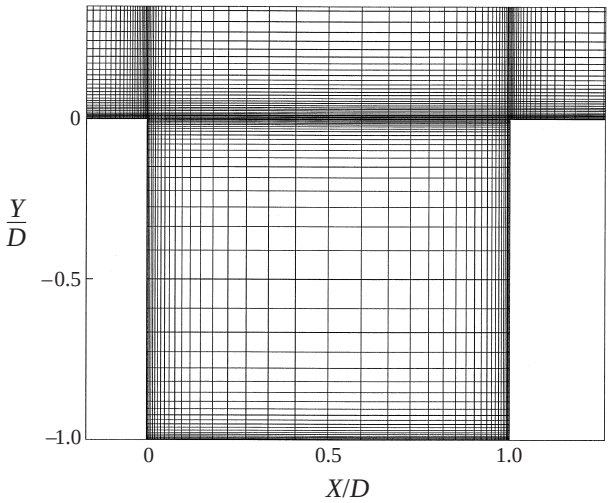

FIGURE 7. Cavity $L/D = 1$. Detail of the computational mesh for the coarsest mesh simulation.

radial distances, X and Y, are normalized by the cavity depth and referenced to zero at the upstream lip, or separation edge, of the cavity. This domain enables a full CFD solution to be carried out on the entire length of the fore-body, since good reproduction of the approach boundary layer and flow field is clearly an important prerequisite to satisfactory modelling of the cavity flow itself. The left-hand side of the domain, just upstream of the model leading edge (at $X/D = -8$), is an inflow boundary at which the appropriate stream conditions are enforced. A transmissive condition is applied at the top boundary. This boundary actually lies outboard of the bow shock wave for most of the chord length, however, so to all intents it usually remains fixed at the stream conditions. The downstream boundary, and body surface, are outflow conditions and no-slip, isothermal (293 K) wall conditions respectively.

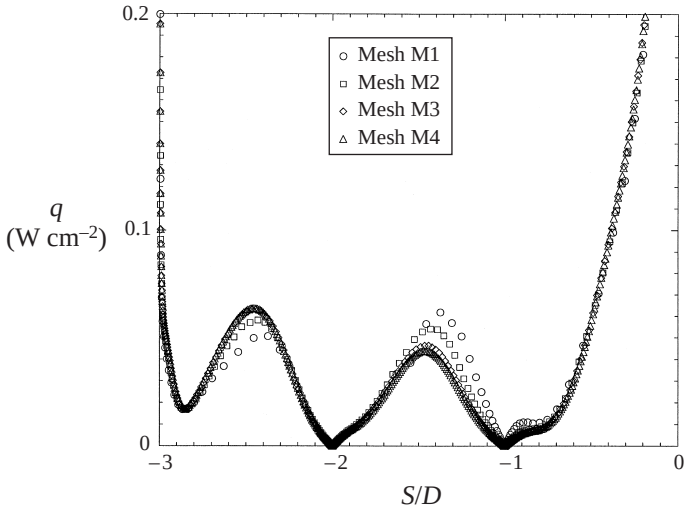

FIGURE 8. Cavity $L/D = 1$. Mesh convergence assessment.

Generally the flow was initialized by employing a simplified representation of the actual firing process of the gun tunnel nozzle, to accommodate as far as possible any effects of flow development history. The pre-firing static test section conditions are 294 K, 0.0019 bar (about 40% of the final test window static pressure), and the flow development to the conditions at the test window is accomplished through a series of strong waves in the first 2 ms, followed by a combination of weak waves and continuous compression of the test gas up to about 10 ms. The computational domain was therefore initialized, everywhere, with the pre-firing conditions, and the inflow boundary conditions were then varied to simulate the nozzle exit flow history. For some computations, especially the finest mesh cases, the computation was initialized by interpolating onto the mesh the converged solution from a coarser mesh calculation. All computations converged to a steady state. Achieving stationary conditions, for separated flow studies in short-duration facilities, is an important issue and will be assessed experimentally in later sections. The computational evolution of the solution also gives some insight, even though the representation of the firing process is only approximate. Figure 6 presents computed histories for the $L/D = 1$ case for pressure, surface skin friction and surface heat transfer, all monitored at the mid-point of the cavity floor ($X/D = 0.5$). Each variable is normalized by its appropriate steady-state value. In this simulation, good steady values are attained in the last few milliseconds of the run, which are normally taken as the data sample window. As expected pressure achieves steady conditions very quickly compared with the viscous controlled processes. Skin friction also reaches its steady state rapidly, so that the basic pressure and velocity fields become quickly established. Heat transfer appears to be the slowest process and it may be that is more sensitive to the actual starting process.

A structured, body-fitted mesh is used, which is rectangular Cartesian downstream of the position where the fore-body becomes parallel ($X/D = -1.08$). To provide good solution resolution, there are two main requirements for the mesh. Firstly, near the body surface, both in the cavity and on the exterior surfaces, and near the free shear layer which bridges the top of the cavity, a fine resolution is required in the local flow-normal direction. This is illustrated in figure 7, which is the coarsest mesh

used for the $L/D = 1$ case, where a stretching of $\pm 5\%$ is used between adjacent cells. A fine resolution is also required in the local flow-tangent direction, however, both to resolve detail near the separation and reattachment lips and also to resolve secondary separation/reattachment detail within the cavity. It is probably the requirement to resolve these secondary eddies (presented in § 6.1), specifically those which appear at the upstream/downstream corners on the cavity floor, which cause the most difficulties in establishing a satisfactory mesh. Figure 8 shows the dependence of the solution on mesh refinement for the $L/D = 1$ case. The coarse mesh (M1), illustrated in part in figure 7, comprises 40 by 40 cells within the cavity, 112 cells along the chord length of the forebody, and 48 cells from the exterior surface of the body to the outer boundary of the domain. Medium (M2) and fine (M3) meshes are constructed as two successive 2 : 1 subdivisions of cells in both the X- and Y-directions. M3 is therefore defined by 160 by 160 cells within the cavity, with a maximum wall-normal dimension for cells adjacent to all body surfaces of only 0.052% of D. Heat transfer is a sensitive test of CFD prediction, and for the exterior model surface the three levels of mesh demonstrate excellent mesh independence; heat transfer predictions for example, at a sample position $1D$ upstream of the separation lip, are within 0.6% of each other for all three levels of mesh. Figure 8 shows the surface heat transfer predictions for the three interior surfaces of the cavity. The wetted distance S is referenced to zero at the rear, reattachment, lip and the negative direction for S is directed clockwise around the cavity surface (also see figure 5 for a general schematic). The main interpretation of the distributions will follow later, but from the viewpoint of mesh convergence there are regions of excellent collapse, and also regions of discrepancy, especially near the maxima on the cavity floor ($S/D \approx -1.5$) and the middle of the front face ($S/D \approx -2.5$). The significance of these regions is that they are the reattachment zones for the secondary corner eddies, seen later in § 6.1 and figure 12. Mesh resolution difficulties, particularly for the coarsest mesh (M1), almost certainly arise because of the sparseness of the mesh interval along the cavity surface rather than lack of resolution in the normal direction (see figure 7). A further mesh, M4, was also tested therefore, to improve the resolution along the surface in these reattachment zones. This did not follow the global subdivision procedure of the previous three meshes, rather it added 80 extra cells to the cavity, in both the x- and y-directions (giving a 240 by 240 mesh), concentrating them in the central 80% of each cavity wall to reduce mesh intervals over this distance and providing reductions in cell size by at least another 2 : 1 factor in the reattachment zone. There is seen to be virtually no further alteration in the predicted heat flux.

Cavity computations were performed up to L/D values of 8, as will be presented later. It was not possible to undertake a comprehensive mesh refinement exercise for each case, but in addition to the shortest cavity just discussed, an assessment was also performed for the $L/D = 4$ case, as shown in figure 9. The three meshes M1, M2 and M3, represent 80 (x-direction) by 40 (y-direction) cells, 160 by 80 and 320 by 160 respectively, with a straight 2 :1 cell subdivision over the whole domain from one mesh to the next. The agreement between all three levels actually seems to be slightly better than for the shortest cavity, especially the prediction of the magnitude of the peak heating on the cavity floor. Meshes M2 and M3 produce very close matching of the detail through the complete cavity. The heat transfer predictions for the two cavities, $L/D = 1$ and $L/D = 4$ would appear, therefore, to be exceedingly close to the mesh-converged solutions. All other cavities have been modelled using a 160 by 80 mesh, that is between levels M2 and M3 in figure 8 and equivalent to level M2 in figure 9.

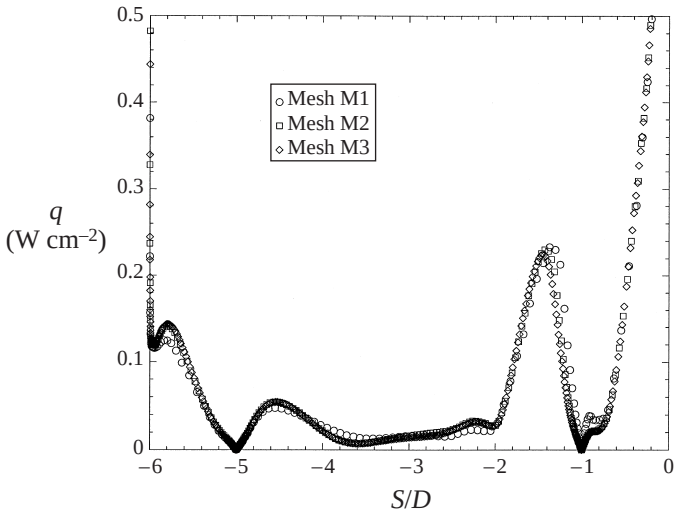

FIGURE 9. Cavity $L/D = 4$. Mesh convergence assessment.

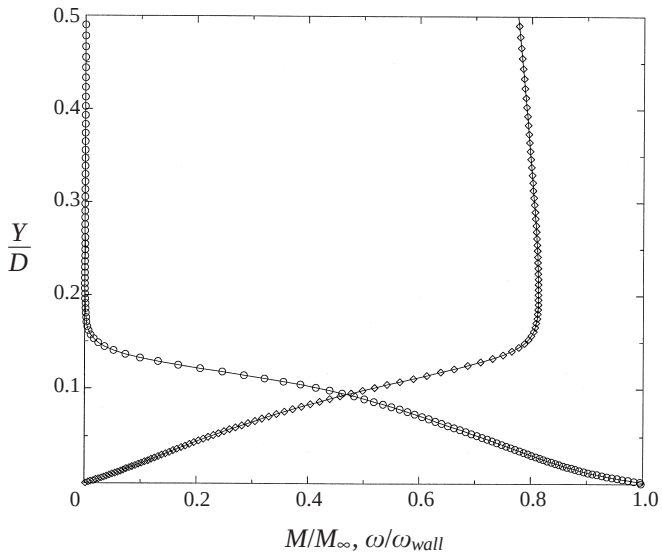

FIGURE 10. Computed boundary layer profiles for Mach number and vorticity at 10 mm upstream of separation ($X/D = -0.4$). M/M_∞ (◇–◇); ω/ω_{wall} (○–○).

5. Fore-body boundary layer and free shear layer transition

Figure 3 shows surface heat transfer for the 'no-cavity' case, measured at stations pitched by 120° around the circumference. Up to $x/D \approx 7$ there is an excellent collapse of data and good agreement with the laminar CFD, confirming that two-dimensionality is achieved within measurement accuracy and that laminar flow can be maintained well downstream of the required separation position. Beyond this distance the experiment and CFD depart progressively with the onset of transition which, for this test model, occurs with a slight asymmetry around the body surface.

The fore-body boundary layer is too thin to measure accurately, so that figure 10 shows computed profile data at a position 10 mm upstream of the separation edge

M_e	δ^*(mm)	δ^*/D	θ (mm)	θ/D	Re_e (m^{-1})	$Re_{\theta,e}$
7.2	2.63	0.1052	0.168	0.00672	4 130 000	694

TABLE 3. Computed laminar boundary layer data just upstream of separation.

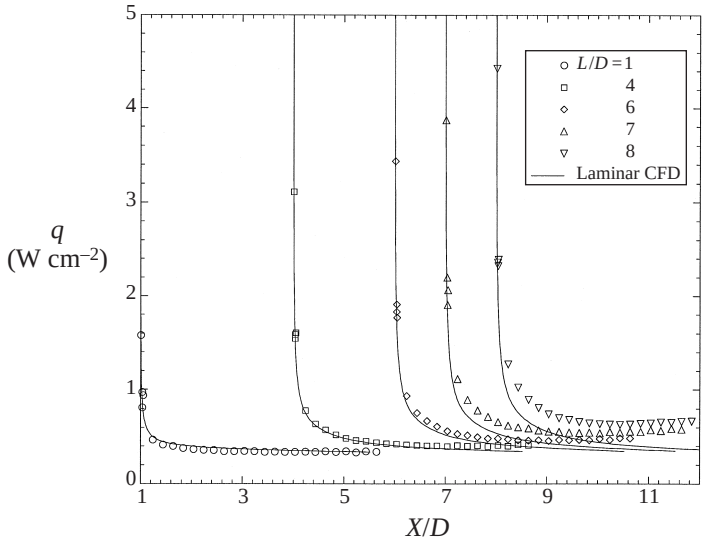

FIGURE 11. Heat transfer distribution on the after-body for various cavity lengths.

($X/D = -0.4$), just ahead of any upstream influence from the cavity. Because of the curvature of the fore-body, and the resultant curvature of the bow shock wave, the flow external to the boundary layer is weakly rotational, though the vorticity is still several orders of magnitude less than the characteristic values in the boundary layer. The resultant integral thicknesses and Reynolds numbers based upon edge conditions are given in table 3. The reduction in unit Reynolds number, compared with that for the free stream, is a direct consequence of the loss of total pressure through the leading-edge shock wave. For similar reasons the boundary layer edge Mach number is approximately 7.2, compared with the free stream value of 8.9, and reduces further outboard until the bow shock wave is reached because of normal gradients associated with the body curvature.

Because of the very thin shear layer, the low gas density and the axisymmetry of the flow field, the schlieren visualization was not sensitive enough to determine the state of the free shear layer. However, for all cavity lengths (up to L/D of 10) it completely bridged the cavity, sometimes referred to as a 'closed cavity' type of flow and there was no photographic evidence of any large-scale unsteadiness. The transition behaviour is best inferred from the surface heat transfer measurements and figure 11 shows after-body data for various cavity lengths. The separation edge (i.e. the upstream side of the cavity) is located at $X/D = 0$ and the axial scale is normalized by the cavity depth, D. For the shortest cavity ($L/D = 1$), with the reattachment lip at $X/D = 1$ therefore, the experiment and CFD are in such close agreement that the reattached flow on the after-body is probably fully laminar over the full measurement length. With increasing cavity length a progressive departure between laminar CFD

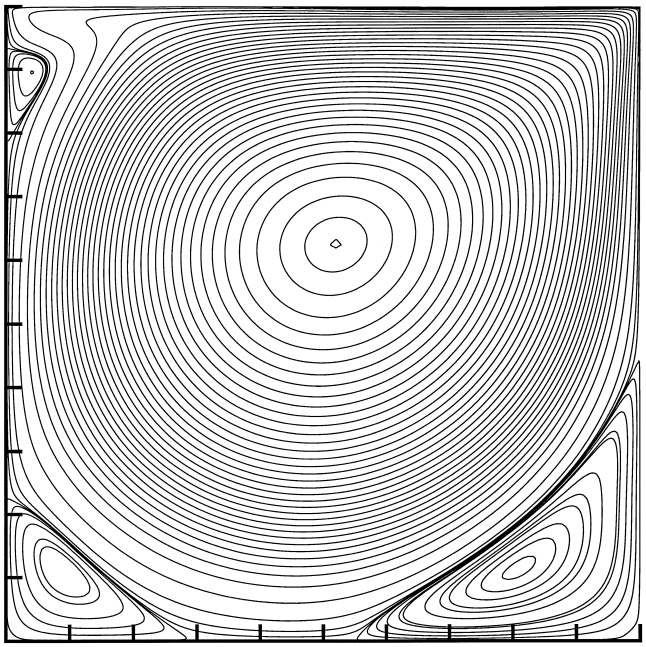

FIGURE 12. Computed cavity streamline pattern for $L/D = 1$. The free-stream flow over the top of the cavity is left-to-right, so that the main cavity vortex has a clockwise circulation.

and experiment becomes apparent, but only for an L/D of 7 or 8 does this departure appear immediately downstream of the reattachment lip. This has to be considered the upper limit for maintaining a laminar free shear layer in these tests.

6. The shortest cavity: $L/D = 1$

6.1. *CFD modelling of cavity streamline pattern*

The streamline pattern of figure 12 shows that the flow is characterized by a primary vortex system, with secondary vortices formed at the two corners between the cavity floor and the front and rear cavity walls. These are denoted as secondary downstream and upstream eddies (SDE and SUE), where 'upstream' and 'downstream' always refer to the sense of the free-stream direction. A small secondary eddy (STE) also forms near the top of the front wall. The resolution of the computation was also sufficient just to detect a tertiary eddy at the downstream corner, underneath the secondary eddy, of order 2% of D in overall scale. Figure 13 shows profiles of vorticity, normalized by the cavity depth, D, and the free-stream velocity, U_∞, taken as horizontal and vertical lines through the centre of the primary vortex. The basic structure of the cavity flow comprises a large central core of virtually constant vorticity, bordered by relatively thin regions of rapid vorticity variation, similar to the basic Batchelor model for separated flows. Considering the horizontal profile the negative vorticity in the region $0.85 \leqslant X/D \leqslant 0.90$ corresponds to the lower part of the reattaching shear layer which is recirculated into the cavity, and the positive vorticity closer to the back face corresponds to the new boundary layer which develops underneath, and diffuses into, this reattaching flow. Defining the thickness of this boundary layer, as it develops with distance down the back face, is not simple. A reasonable definition is to locate its edge at the local minimum of vorticity. Figure 14 shows the development of this thickness,

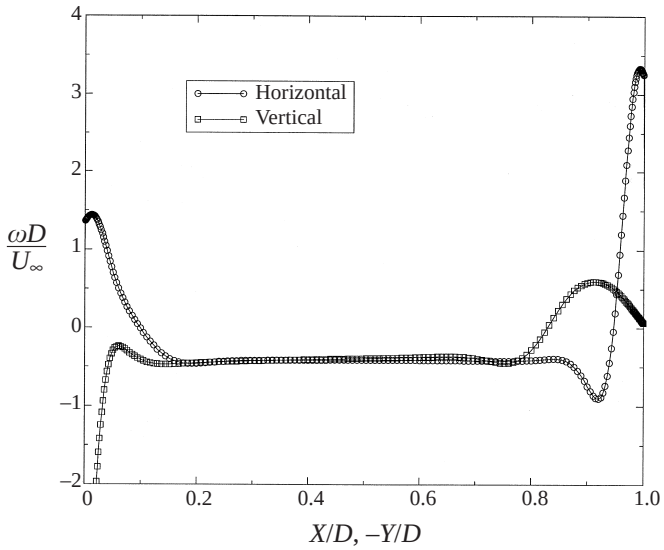

FIGURE 13. $L/D = 1$. Profiles of vorticity, taken horizontally and vertically, through the centre of the primary vortex.

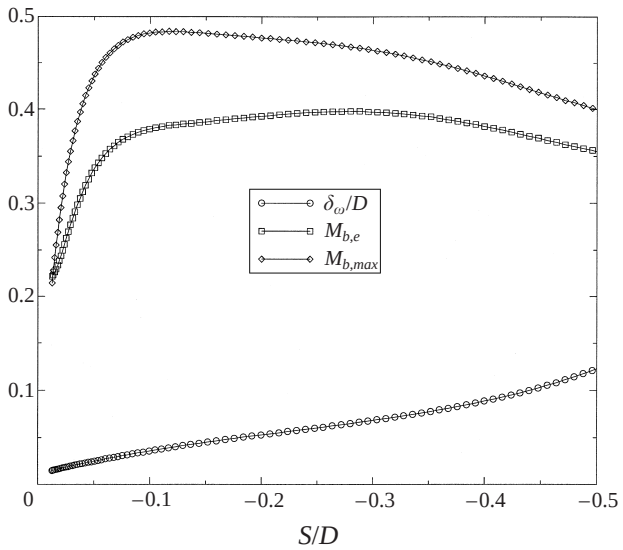

FIGURE 14. $L/D = 1$. Boundary layer development with distance, S/D, down the cavity back face. The position $S/D = 0$ corresponds to the reattachment lip.

δ_ω, with distance (S/D) down the back face, and also the associated variation of boundary layer 'edge' Mach number, $M_{b,e}$. The maximum downflow velocity in the back face boundary layer occurs slightly inboard of its edge so that figure 14 also includes the corresponding distribution of the maximum Mach number, $M_{b,max}$. The highest Mach number achieved is about 0.48 at $S/D = -0.1$, compared with a maximum Mach number on the dividing streamline, $M_{d,max}$, of 0.72 (see figure 15). The computed trajectory of the dividing streamline is very flat and separation and reattachment are both predicted to occur slightly below the upper lips of the front

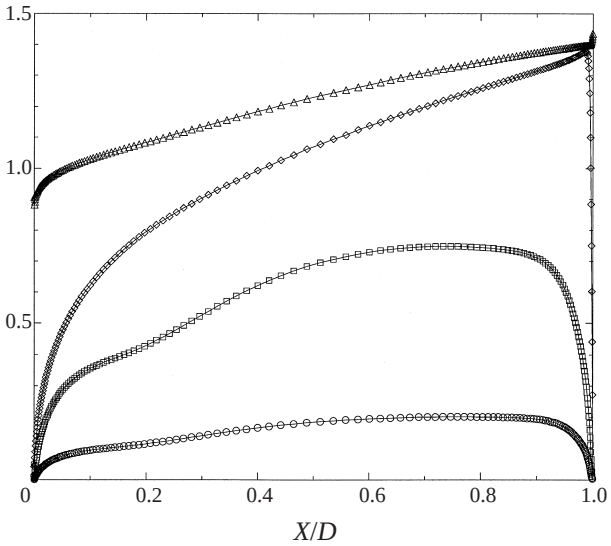

FIGURE 15. $L/D = 1$. Variation of flow properties along dividing streamline. U/U_∞ (○–○); P_0/P_∞ (△–△); $(T_0 - T_w)/(T_{0,\infty} - T_w)$ (◇–◇); M (□–□).

and back faces respectively, but nowhere does the dividing streamline depart by more than 0.4% of D from the line connecting the two cavity lips. In the present situation the state of the free shear layer is still strongly dependent on the characteristics of the boundary layer just upstream of separation. A large development length would be required – much longer than the cavity length (L) – for the shear layer to become independent of this influence. This development length (for the plane shear layer) is modelled in various papers, such as those of Denison & Baum (1963), Kubota & Dewey (1964) and Charwat & Der (1966). Kubota & Dewey (1964), for example, express the growth of a plane, compressible laminar free shear layer in terms of the parameter $(x/\theta)(Re_{\theta,e})^{-1}$, where θ is the boundary layer momentum thickness at separation and x is the shear layer development length. By reattachment on the downstream cavity wall in the present study this parameter has reached a value of only 0.24, whereas Kubota & Dewey (1964) indicate that values at least an order of magnitude larger are necessary for the laminar free shear layer to approach an asymptotic state. Because of the low Mach number for the dividing streamline and the cavity a comparison with low-speed studies is worthwhile. The corresponding 'free shear layer' case is not appropriate, because it is highly unsteady, but comparison with a lid-driven cavity flow is relevant instead. An 'equivalent' lid-driven cavity Reynolds number of 1120 is obtained using the cavity depth and the computed flow conditions at the maximum velocity position on the dividing streamline. The location and scale of the primary and secondary vortices in figure 12 are virtually identical to those predicted by incompressible simulations and experiments for planar lid-driven cavities at similar Reynolds numbers (for example Ghia, Ghia & Shin 1982; Kim & Moin 1985; Koseff & Street 1984; Ramanan & Romsy 1994).

6.2. *Experimental study of cavity flow establishment time*

The flow establishment time is an important consideration for separation studies in transient facilities, studied by Rom (1963), Ihrig & Korst (1963), Holden (1971) and Mallinson, Gai & Mudford (1997*a*) amongst others. It is controlled by acoustic

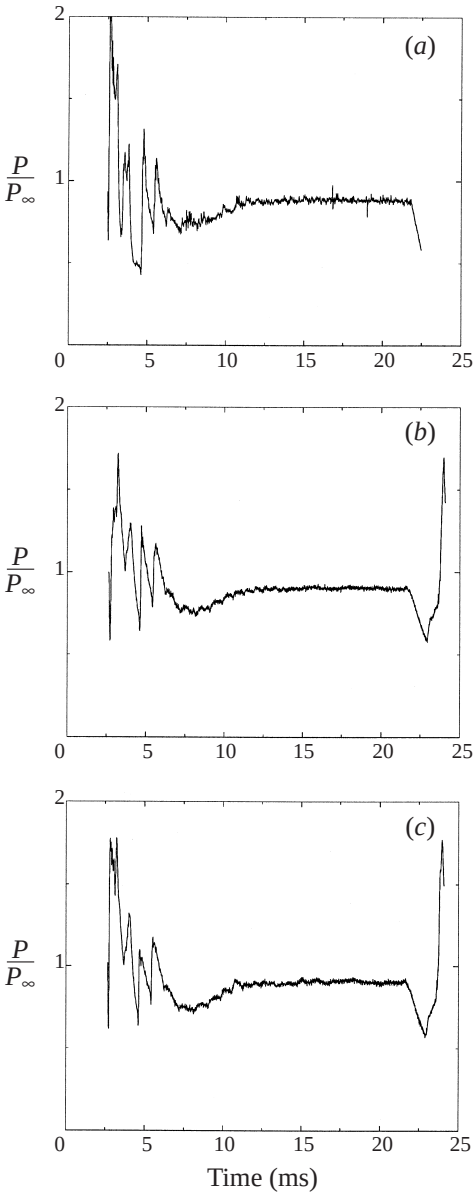

FIGURE 16. $L/D = 1$. Sample pressure histories. (*a*) mid-height of cavity back-face; (*b*) cavity floor at $X/D = 0.28$; (*c*) cavity floor at $X/D = 0.68$.

wave propagation, flow convection and viscous diffusion and since the latter is the slowest process heat transfer histories were the primary means of assessment here. The following concerns only the shortest cavity ($L/D = 1$) and the longer cavities will be considered later in § 7.

First, however, figure 16 indicates the establishment of surface pressure using pressure histories, from a single experimental run, at the mid-point of the cavity back face and at two positions on the cavity floor. The time-origin is at 2.5 ms on these traces and the tunnel flow breaks down at 21.5 ms. All traces show a substantial period

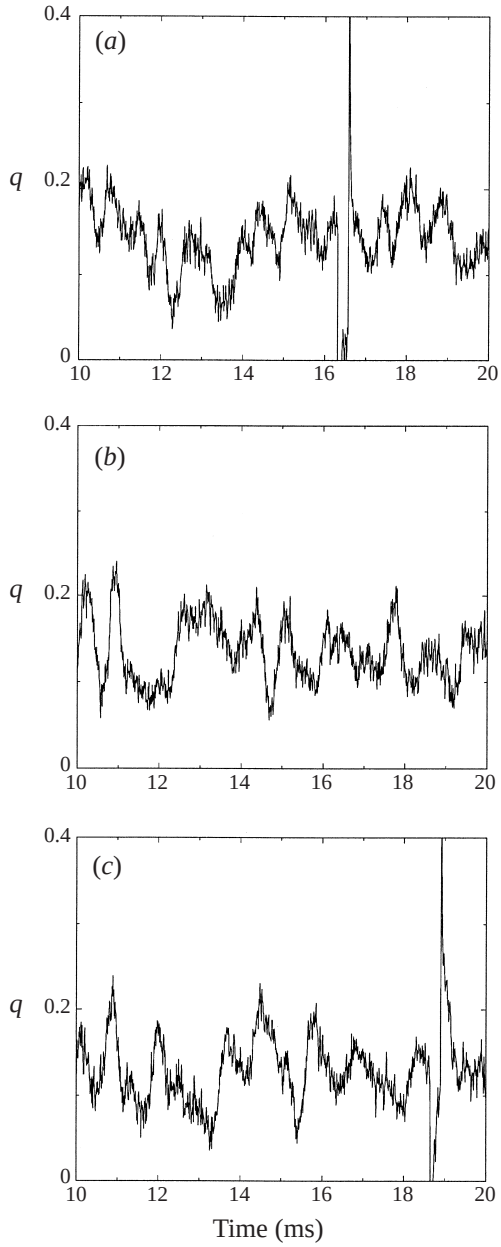

FIGURE 17. $L/D = 1$. Three sample heat transfer histories on cavity floor at $X/D = 0.68$.

during which a mean value can be readily determined. An 8 ms window corresponds to convection of the free stream by nearly five hundred cavity lengths, although the physically significant velocity scales for cavity flows are clearly much lower than this. During this phase there are small fluctuations in pressure about the mean, whose r.m.s. amplitude is approximately 1% to 2% of the mean cavity pressure, about 3% of the maximum dynamic head on the dividing streamline.

The heat transfer data require more careful consideration. Signal levels are very small and place considerable demands on measurement accuracy. The maximum heat

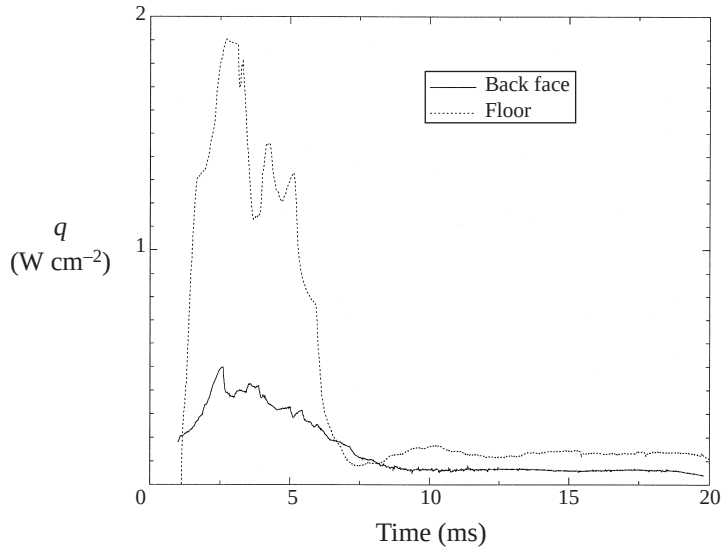

FIGURE 18. History of 2.5 ms running average of heat transfer at the middle of the back face and on the cavity floor.

flux on the cavity floor is less than 25% of the equivalent values for the attached boundary layer which (at 0.4 W cm^{-2}) is already low. In addition all locations showed distinct unsteadiness, with the impression that the largest relative fluctuations possibly occurred on the cavity floor. Figure 17 shows three sample time-histories, all taken in successive runs at the same position on the cavity floor. In each case the first 10 ms of the run is excluded, since very large starting transients occur during this period. The fluctuation amplitude is of the same order as the mean value and in two of the traces large narrow-band excursions in heat transfer occur. These are possibly aerodynamic in origin although instrumentation or gauge 'erosion' effects cannot be discounted. Normally data are averaged over a 2.5 ms sample near the end of the run, and are then further averaged over three successive runs. To assess whether this is adequate figure 18 shows time-histories of 2.5 ms running-averages, which are also averaged over three identically triggered runs (using the records of figure 17 in the case of the cavity floor). The tunnel start-up causes significant variations up to 10 ms from the initial 'trigger', but the signals then remain nearly constant over the remainder of the run. Despite the high amplitude of the fluctuations, and their low frequency, which will be considered further in § 6.3, the run time appears sufficient to establish a stationary state.

6.3. *Surface distributions of pressure and heat transfer*

Figure 19 presents the mean surface pressure and heat transfer distributions, experimental and computational, for the cavity and parts of the fore-body and after-body. The distance axis, S, represents a wetted distance along the body surface, referenced to zero at the top rear corner of the cavity and normalized by the cavity depth D, as illustrated in figure 5. Thus the reattachment and separation lips are at $S/D = 0$ and $S/D = -3.0$ respectively. No pressure data were obtained on the front face of the cavity ($-3.0 \leqslant S/D \leqslant -2.0$). The computations for pressure show excellent agreement with experiment, both close to the reattachment lip and also on the cavity floor. The

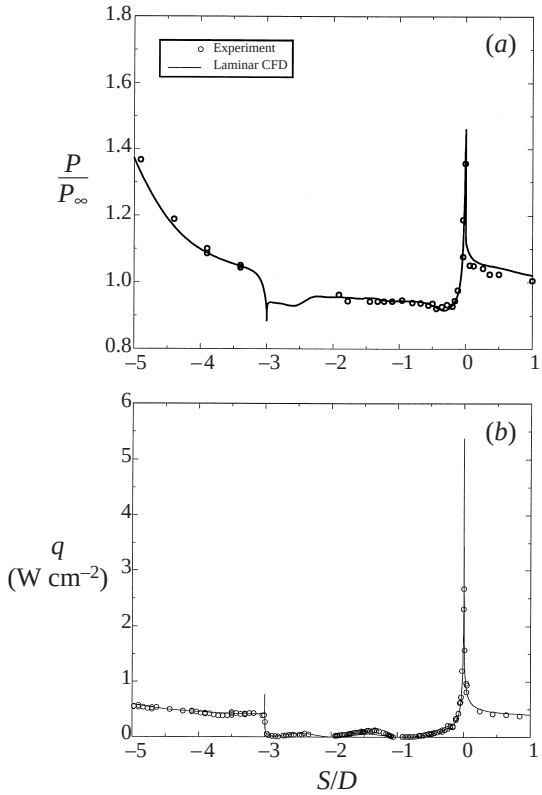

FIGURE 19. $L/D = 1$. (*a*) Surface pressure distribution. (*b*) Surface heat transfer distribution.

computed pressure distribution, compared with the 'no-cavity' case of figure 3, also indicates an upstream influence from the separation edge, about $0.2D$ in extent.

The heat transfer data represent a very comprehensive set of measurements, both in the fine increment in S/D and also because data are recorded at various circumferential stations. On the back face of the cavity, for example, four radial rows of sensors were used, pitched at 90° around the circumference. The very low scatter is a measure of the high quality of axisymmetry achieved for the time-averaged data. The detail of the distribution is shown better by figures 20(*a*) and 20(*b*) which focus, respectively, on the vicinity of reattachment and on the interior surface of the cavity. Even then, gradients on the front and rear faces of the cavity, close to separation and reattachment respectively, are so steep that localized distributions are shown in figures 20(*c*) and 20(*d*) for distances of only $\pm 0.1D$ (± 2.5 mm) from the lips. Agreement between experiment and the laminar CFD is excellent on the fore-body, after-body and rear-wall of the cavity, and almost as good on the instrumented part of the forward face of the cavity ($-3.0 \leqslant S/D \leqslant -2.3$).

On the floor of the cavity there are marked discrepancies between measured and computed heat transfer (see figure 20*b*), however. The difference appears slightly upstream of the downstream corner, for the region $S/D \leqslant -1.1$, and extends at least as far as the upstream corner, $S/D = -2.0$. Possibly it also extends up the lower part of the front face as well, but by the first measurement point on this face agreement is good again (also see figure 20*d*). Almost certainly the difference has to be connected with the unsteadiness in heat transfer noted earlier in figure 17. More

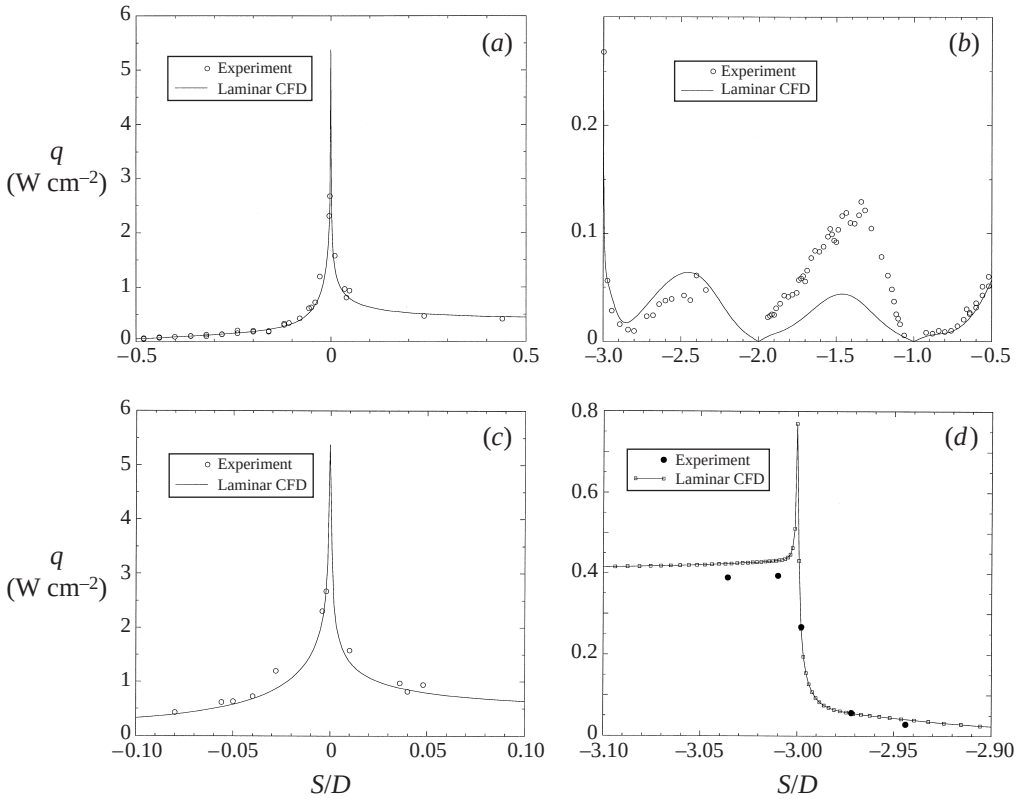

FIGURE 20. $L/D = 1$. Heat transfer detail on (*a*) the cavity back face and after-body, (*b*) the cavity floor, (*c*) very close to the reattachment lip, and (*d*) very close to the separation lip.

specifically, given that the two-dimensional time-accurate laminar CFD simulations reach a steady state and that the time-averaged experiments are two-dimensional, the cause seems to be either that the flow on the cavity floor is turbulent or, though still laminar, that it is three-dimensionally unsteady. There is ample evidence, both experimental and computational, that lid-driven cavity flows experience three-dimensional instabilities, probably originating as the primary cavity vortex flows over the lower secondary eddies. These are documented, for example, in Aidun, Triantafillopoulos & Benson (1991), Koseff & Street (1984), Kim & Moin (1985), Ramanan & Romsy (1994) and others. Periodic three-dimensional unsteadiness first appears in the Reynolds number range 500–1000 (based upon lid velocity and cavity depth), developing into Taylor–Görtler-type vortices (with transverse scales of order half the cavity depth) which eventually 'burst' or break down to turbulence. There is no precise correspondence between the 'equivalent' Reynolds number of 1120 defined earlier in § 6.1, for the present cavity flow, and the definition for lid-driven flows, but the conditions are consistent with the present study being close to or above the threshold for the onset of three-dimensional unsteadiness. The flow would then be similar to the cellular streamwise structures shown by Roshko & Thomke (1966), for the reattaching flow downstream of a rearward-facing step, but with an unsteadiness associated with irregular spanwise motion of the vortex structures. The characteristic time scale for the fluctuations is of order 1 ms, so that a reduced time $\tilde{t} = tU_d/D$, based upon the maximum computed velocity (figure 15) on the dividing streamline

U_d, is about 11.0. Reduced fluctuation periods for lid-driven cavities have been estimated from numerical simulations and from experiment and seem to encompass a large range. Linear stability calculations by Ramanan & Romsy (1994) and Ding & Kawahara (1998) predict a critical non-dimensional period $\tilde{t}$ (based on the lid velocity) of order 10.0, for the planar cavity with infinite (spanwise) aspect ratio, and experiments by Aidun *et al.* (1991) show a value for $\tilde{t}$ of 9.0 for the periodic state. Experimental studies also indicate that spanwise aspect ratio, that is the presence of a solid sidewall, has a significant effect upon the mean eddy structure (Koseff & Street 1984) and characteristic period (Chiang, Sheu & Hwang 1998). Nonetheless, the quoted values are all comparable to those inferred here. In a lid-driven flow, disturbances clearly have to originate in the cavity. In the present study there is an additional mechanism in that perturbations of the reattaching shear layer, driven by free-stream disturbances, feed directly towards the cavity floor. The extreme thinness of the reattaching shear layer makes this an effective amplification process.

6.4. *The dividing streamline and conditions near separation and reattachment*

Since the departure between CFD and experiment is confined to heat transfer predictions on the cavity floor, the streamline predictions of figure 12 should still be realistic for the bulk of the cavity. Figure 15 shows the predicted variation of various properties along the dividing streamline. Goldstein (1930) showed that the velocity in the incompressible near wake of a flat flate behaves as $x^{1/3}$ and this scaling also featured in the compressible free shear layer models of Denison & Baum (1963) and Charwat & Der (1966). The initial dividing streamline velocity in figure 15 follows this scaling fairly well, despite the underlying differences associated with the cavity recirculating flow. The computed heat transfer on the fore-body shows a narrow peak just prior to separation (see figure 20*d* for example). This is not a numerical problem, but rather a real feature associated with the near-wake separation behaviour which was revealed increasingly over the three successive mesh refinements M1, M2 and M3 (M4 has the same mesh structure as M3 in this zone) presented earlier in § 4 – though the finest, shown here, is still not sufficient to resolve its magnitude fully. Measurements were not possible on the fore-body sufficiently close to the separation edge, but the same singular behaviour is also apparent on the front face of the cavity (figure 20*d*). Here measurement was possible very close to the edge, with an excellent correspondence between computations and the three experimental points in the interval $-2.99 \leqslant S/D \leqslant -2.95$.

The streamline patterns of figure 12, and also skin friction predictions on the back face, indicate that reattachment occurs at $S/D \approx -0.004$. This is only four cell-widths from the lip of the reattachment face, so that the relative position is not well resolved computationally although it is sufficient to confirm that reattachment does not occur at the lip itself. The main deceleration along the dividing streamline (figure 15) occurs within a distance of order $0.1D$ of the wall. This indicates the extent of the upstream influence of the stagnation zone, effectively some measure of the local free shear layer thickness, and therefore related to the reattachment length scale Δ of Chung & Viegas (1961), Hodgson (1970) and others, which will be considered further in § 7.3. The total pressure is little changed over this distance, as expected. The fall in total temperature to the wall value at reattachment gives a measure of the thickness of the new boundary layer, δ_ω, formed in the reattachment zone (see figure 14) and effectively an order of magnitude less in scale than Δ.

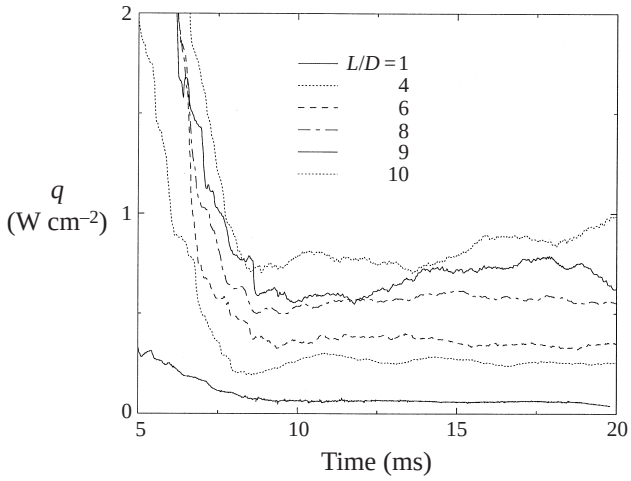

FIGURE 21. Flow establishment characteristics for various length cavities, measured at the mid-height of the cavity back face.

7. The effect of increase in cavity length

7.1. *Flow establishment*

Figure 21 shows 2.5 ms 'running-average' time-histories, generated in the same manner as those shown earlier in figure 18, for heat transfer measured on the cavity back face, for a range of cavity lengths. The first 5 ms of the response is excluded since very large excursions in heat transfer occur during the flow starting process. For L/D values up to 8, the cavity flow becomes fully established before the end of the test flow at about 20 ms. For larger L/D values this is not the case, however, so that the data will be restricted to a maximum L/D of 8.

7.2. *Computed cavity streamline patterns*

Increasing L/D from 1 (figure 12) to 1.5 (figure 22(*a*)) is associated with the growth, and amalgamation, of the secondary upstream eddy and the secondary top eddy. This amalgamated eddy continues to grow with further lengthening of the cavity, seen in figures 22(*b*) and 22(*c*) for L/D of 2 and 4. The original primary eddy is little changed in scale during this process so that the dominant motions (and hence the peak cavity floor heating rates) remain located close to the rear of the cavity. Figure 23, for example, shows the variation of vorticity across the mid-height of the cavity for the $L/D = 4$ case. The two main vortex systems correspond to virtually constant vorticity zones, with the largest variations associated with the shear flow between them and also the flow in the endwall boundary layers. It should be noted that the streamline contour intervals do not represent equal increments, rather they have been selected to highlight various features. Thus the eddy trapped near the middle of the cavity floor in figure 22(*c*), with clockwise circulation, is very weak compared with the primary system; the maximum computed reverse flow velocity is only 0.3% of that of the free stream. The back face boundary layer thickness, δ_ω, defined in the same manner used for figure 14, is shown in figure 24. The profile is terminated at $S/D = -0.5$, since the boundary flow is approaching the separation position of the secondary downstream eddy. The maximum downflow Mach number $M_{b,max}$ has risen to 0.7, from the value of 0.48 found for the $L/D = 1$ case. For the longest cavity calculated, $L/D = 8$, $M_{b,max}$ is 0.84.

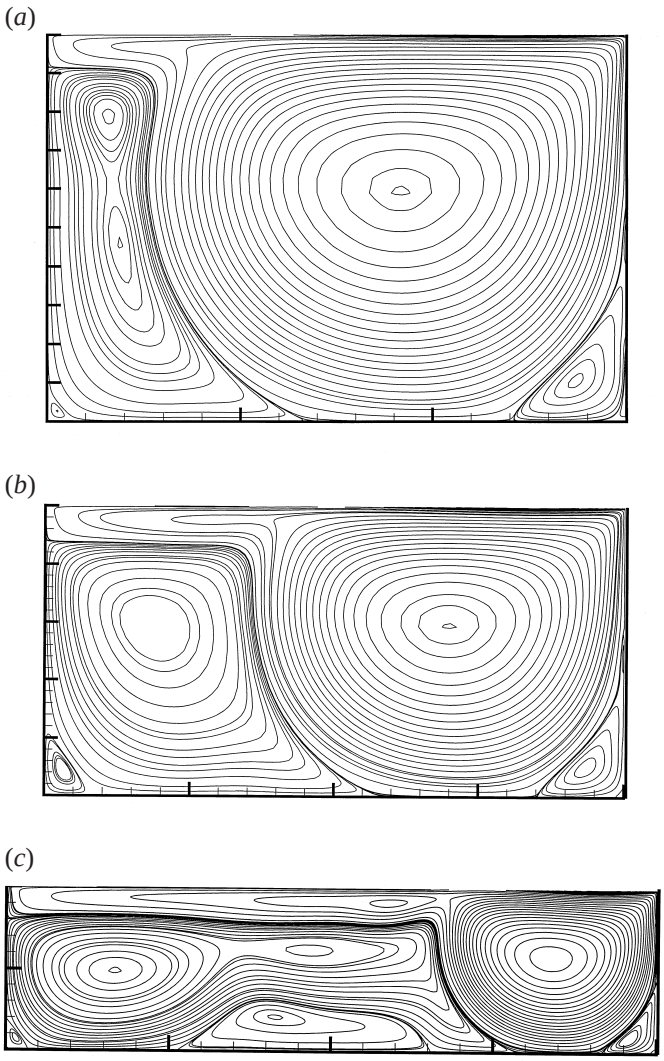

FIGURE 22. Computed cavity streamline pattern for (*a*) $L/D = 1.5$, (*b*) $L/D = 2$, (*c*) $L/D = 4$.

7.3. *Surface pressure and heat transfer data*

The development of the discrepancy between experiment and CFD, noted on the floor for the shortest cavity, can be seen in figures 25 and 26 for a doubling in cavity length.

The region of discrepancy now covers the entire floor of the cavity, the lower part of the back face of the cavity and the forward face as well. The measured heat transfer at the downstream corner between the cavity floor and the back wall ($S/D = -1.0$) is also non-zero. This contrasts with the computations, which show that for all cavity lengths the heat transfer tends to zero at the upstream and downstream corners. A zero corner value can probably be taken as a defining feature for a steady, two-dimensional, laminar cavity flow and indeed a zero value effectively occurs in the experimental data at the downstream corner for the shortest cavity ($L/D = 1$) in figure 20(*b*). With further elongation of the cavity the discrepancy penetrates progressively up the back

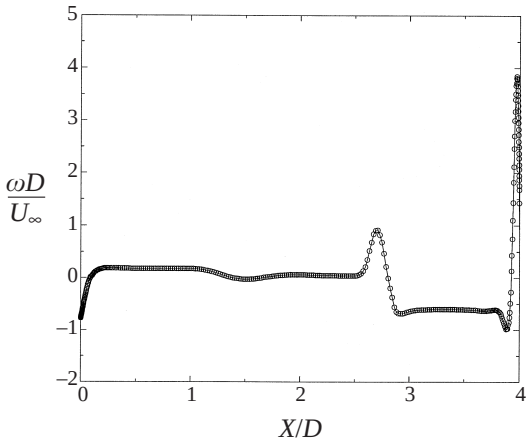

FIGURE 23. $L/D = 4$. Vorticity profile across the cavity at $y/D = -0.5$.

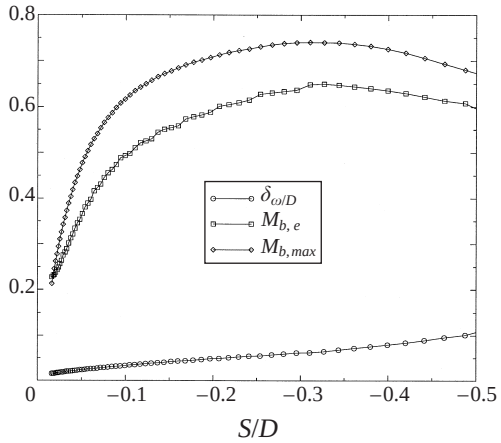

FIGURE 24. $L/D = 4$. Boundary layer development on the back face.

face ($-1.0 \leqslant S/D \leqslant 0$), as shown in the sequence of figures 27, 28 and 29 for values of L/D up to 5.

For L/D values of 6, 7 and 8 it was only possible to record data on the front and back faces of the cavity and figure 30 shows that the discrepancy between experiment and laminar computations now grows rapidly, eventually extending to the reattachment lip and onto the after-body. As noted in § 5, almost certainly the reattaching free shear layer is transitional by $L/D = 8$, but it is not clear how or whether this is actually linked with CFD/experiment discrepancies. It is also interesting to note that it was for the L/D values of 9 and 10 (see figure 21) that it became difficult to establish an acceptable steady state. For the shorter cavities, where the reattaching flow is contaminated neither by the onset of free shear layer transition nor by the encroachment of three-dimensionality from the cavity floor, it is appropriate to attempt to correlate surface heat transfer near the reattachment lip in terms of local flow variables, in the spirit of the approximate theories of Chung & Viegas (1961) and Hodgson (1970). We therefore consider the dependence $St_d\sqrt{Re_{\Delta,d}} = fn(S/\Delta)$ where S is the wetted distance from the reattachment lip and the length scale Δ is obtained

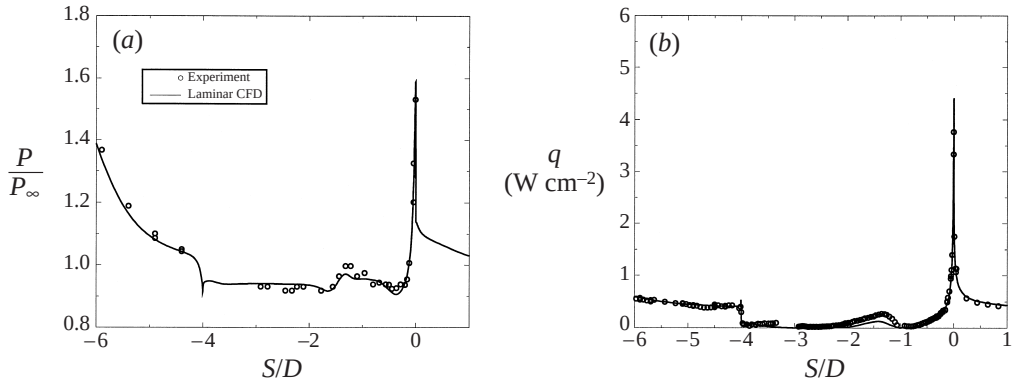

FIGURE 25. $L/D = 2$: (*a*) surface pressure distribution, (*b*) surface heat transfer distribution.

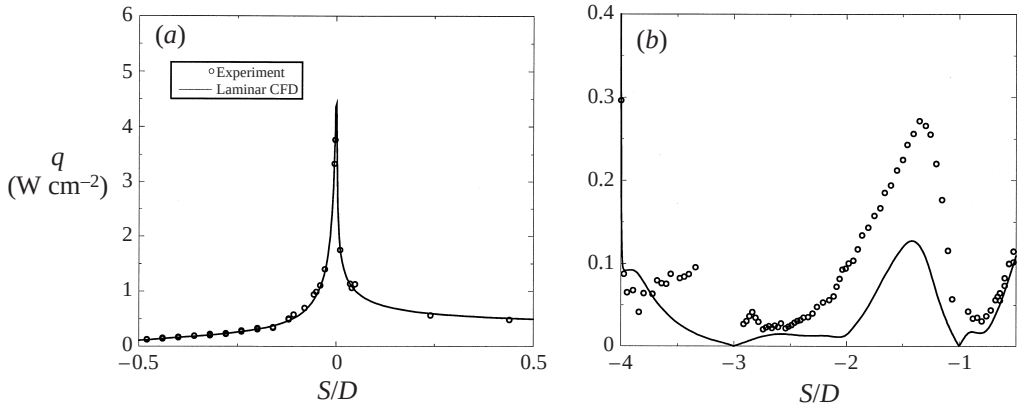

FIGURE 26. $L/D = 2$. Detail of surface heat transfer distribution: (*a*) near reattachment lip, (*b*) back face, floor and front face.

from the computational solutions as $\Delta = U_d/\omega_d$ with the velocity U_d and vorticity ω_d evaluated on the dividing streamline at the position where U_d is a maximum. Figure 31 shows the resultant variation of Δ with cavity length. St_d is also calculated using the computed conditions at the maximum velocity position on the dividing streamline, as $St_d = q[\rho_d U_d Cp(T_{r,d} - T_w)]^{-1}$, where q is the measured surface heat transfer and the recovery temperature $T_{r,d}$ is based on a recovery factor r of $Pr^{1/2}$. Figure 32 includes data on both the cavity back face ($S \leqslant 0$) and the after-body immediately downstream of the reattachment lip ($S \geqslant 0$), since both regions are dependent on the local shear layer structure, though the theories of Chung & Viegas (1961) and Hodgson (1970) are only developed for the back face, however. The experimental data collapse very well for L/D values up to 5 or 6, but for the longer cavities a departure from the correlation is apparent, reflecting the various factors discussed earlier. The theoretical prediction of Hodgson (1970) tends to underpredict the severity of the gradient of the distribution. The surface pressure on the cavity back face should presumably also show a dependence upon the reattachment length scale. Figure 33 presents the data in the form $Cp_d = (p - p_\infty)/(P0_d - p_\infty) = fn(S/\Delta)$, where $P0_d$ is the computed maximum total pressure on the dividing streamline. The data collapse near the reattachment lip is good, but for the longer cavities a distance $S/\Delta = -2$ or -3

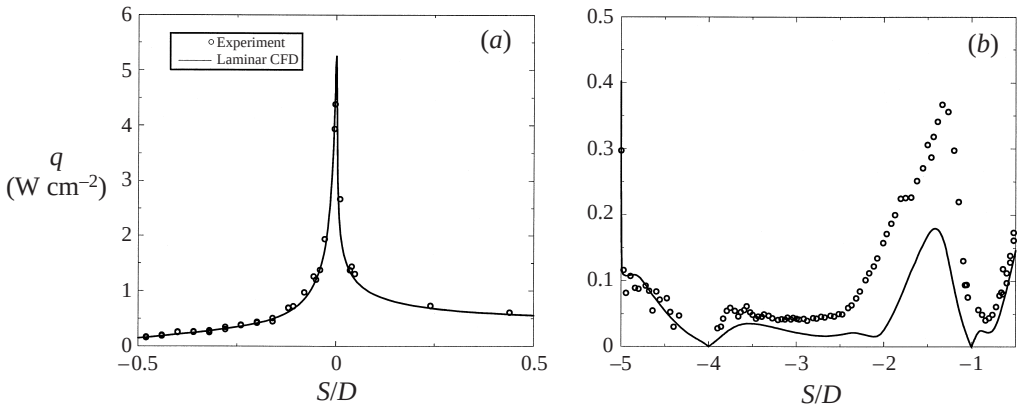

FIGURE 27. $L/D = 3$. Detail of surface heat transfer distribution: (*a*) near reattachment lip, (*b*) back face, floor and front face.

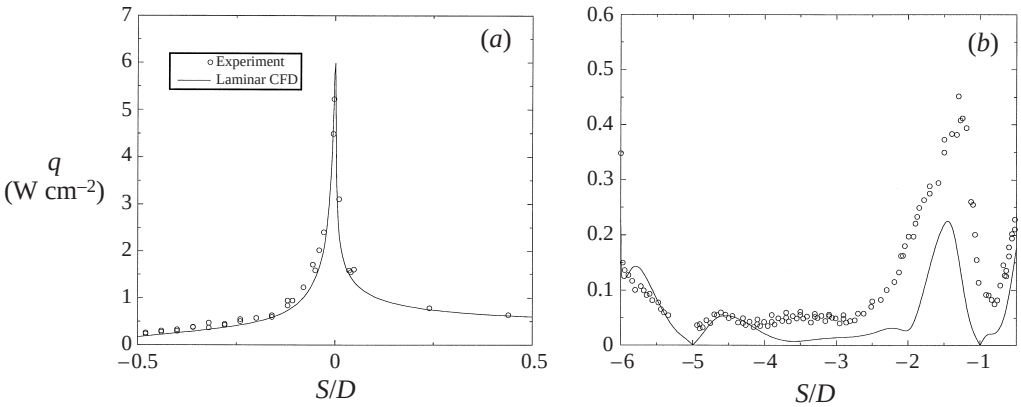

FIGURE 28. $L/D = 4$. Detail of surface heat transfer distribution: (*a*) near reattachment lip, (*b*) back face, floor and front face.

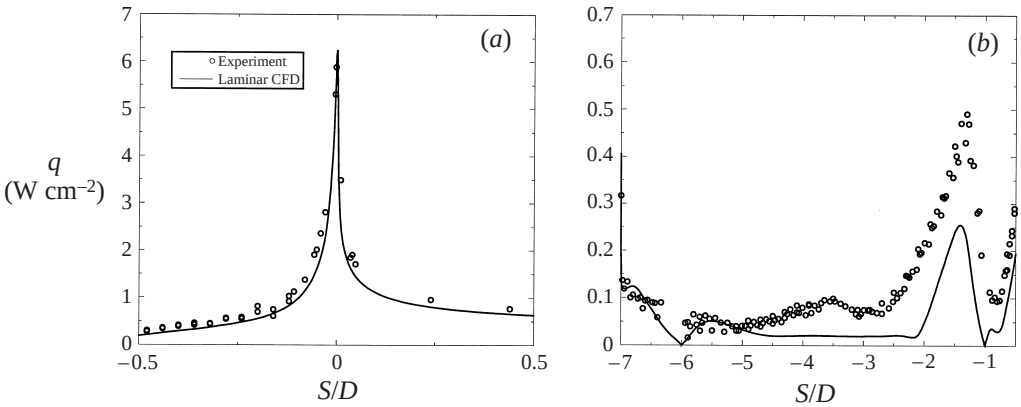

FIGURE 29. $L/D = 5$. Detail of surface heat transfer distribution: (*a*) near reattachment lip, (*b*) back face, floor and front face.

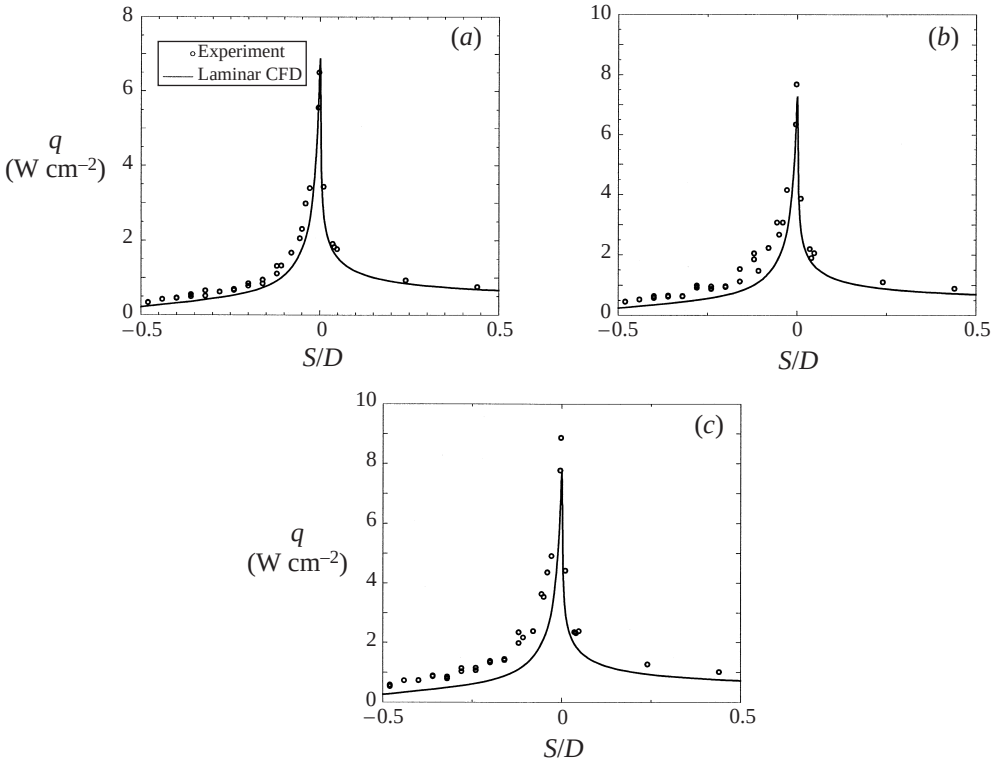

FIGURE 30. Detail of surface heat transfer distribution on cavity back face. (*a*) $L/D = 6$; (*b*) $L/D = 7$; (*c*) $L/D = 8$.

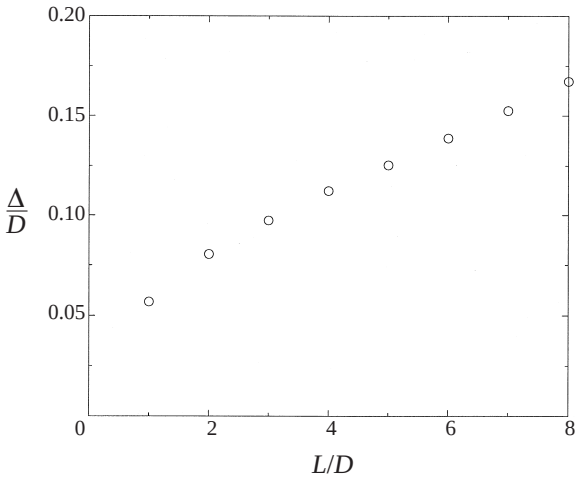

FIGURE 31. Variation of computed shear layer reattachment length scale Δ with cavity length.

means that the measurement location is entering the secondary downstream eddy, so that any correlation cannot be expected to be dependent only on local reattachment variables and this appears to be the case – though this observation obviously should apply to the heat transfer data as well. It should also be noted that the pressure falls

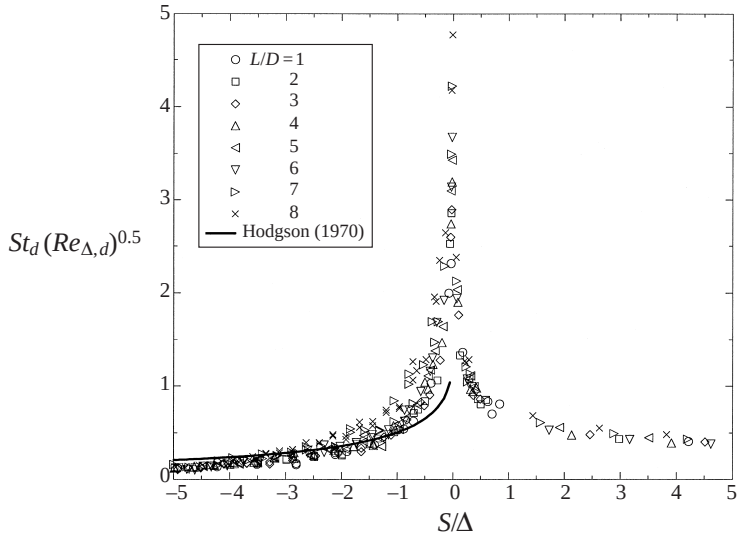

FIGURE 32. All values of L/D. Correlation of measured reattachment heat transfer distribution.

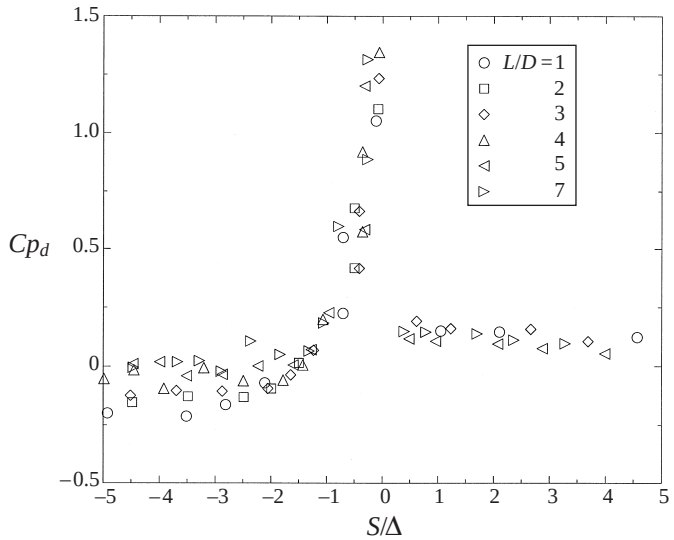

FIGURE 33. All values of L/D. Correlation of measured reattachment pressure distribution.

very rapidly as the flow expands around the reattachment lip onto the afterbody, again well supported by the computations (see, for example figure 19 and figure 25) which also indicate that no separation of the flow occurs at this corner.

On the cavity front face, agreement between experiment and computation is generally good for all cavity lengths, apart from the $L/D = 2$ case, which is probably sensitive to the rapid changes in the cavity vortex systems which were shown in figure 22(a, b). The effect of the separation edge singularity is also reproduced well by both the CFD and experiments for data on the cavity front face. The major discrepancy between experiment and computation is on the cavity floor and for all cavity lengths the peak experimental measurement appears to be nearly twice the

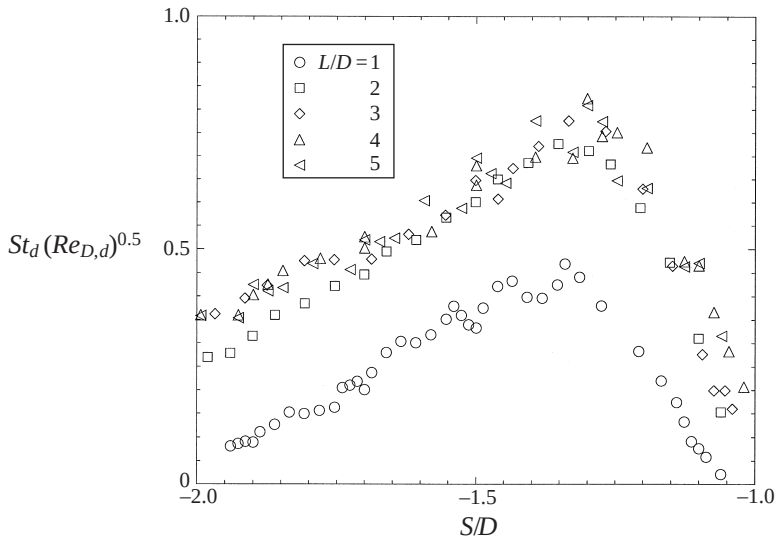

FIGURE 34. All values of L/D up to 5. Correlation of measured heat transfer on the cavity floor near the back face.

computed values and located slightly downstream (in the sense of the free-stream direction) of the computational peak. By L/D of 4, the peak heating on the floor exceeds the equivalent attached boundary layer value. The agreement in positioning certainly suggests that the computed position for the primary vortex system is correct, and that peak heating on the floor occurs close to the reattachment of the shear layer between the primary vortex and the secondary downstream eddy. These heating rates will be dependent upon the dividing streamline flow conditions, though it seems less likely that the shear layer reattachment length scale Δ would be of importance. The appropriate length scale might be a measure of the development length of the boundary layer down the back face, and over the secondary eddy, so that the data (in the interval $-2 \leqslant S/D \leqslant -1$) are plotted in figure 34 as $St_d\sqrt{Re_{d,D}} = fn(S/D)$, where St_d again uses flow conditions at the maximum velocity position on the free shear layer as defined above but the Reynolds number is now defined using the cavity depth (D) with flow properties evaluated on the dividing stream line (d). Apart from the shortest cavity length this produces a surprisingly good collapse of the data, perhaps suggesting that for $L/D \geqslant 2$ the 'cellular' flow on the cavity floor is established, but that the shortest cavity is in transition between a truly two-dimensional flow and the unsteady three-dimensional state. As likely an explanation, however, is that the shortest cavity length is also a special case since the primary vortex is confined by the cavity front face (as well as the back face) in a way that clearly does not arise for any of the other cavity lengths.

8. Concluding remarks

Using a body of revolution, the experiments have produced an excellent standard of two-dimensionality for the mean flow field, for all cavity lengths, which is unlikely to be matched by any equivalent planar configurations. For the shorter cavities, the good agreement between experiment and laminar CFD on the front and back faces of the cavity, together with the fore-body and after-body, is strong evidence for laminar

flow. The flow unsteadiness, and the disagreement between CFD and experiment on the cavity floor, is a significant (and ultimately dominating) feature. Despite studies (computational and experimental) which indicate two-dimensional unsteadiness for cavity flows, there is no reason to believe that this is the mechanism here: there was no evidence in flow visualization of any large-scale shedding from the cavity; heat transfer fluctuations are not regular and their characteristic period is much less than that indicated for cavity resonance (see Rossiter 1966 and Zhang 1995 for example); recirculation speeds in the cavity are also significant compared with the local speed of sound so that there does not seem to be a mechanism to permit good spanwise correlation of fluctuations. The unsteadiness is far more consistent with unsteady Görtler-type vortices or cellular patterns, identified in many theoretical and experimental studies for lid-driven cavities at comparable cavity Reynolds numbers, and also in other separation studies such as those of Roshko & Thomke 1966. The nature of the correlation in figure 34 would suggest that this cavity floor boundary layer behaviour is probably laminar as well.

This work was funded by joint grants from EPSRC and MoD DERA and this support is gratefully acknowledged. Our thanks are also due to Mr Roland Hutchins for his excellent craftmanship in model and instrumentation manufacture and for the operation of the wind tunnel. We would also like to thank Mr Amer Sheikh for his assistance in preparing the figures.

REFERENCES

Aidun, C. K., Triantafillopoulos, N. G. & Benson, J. D. 1991 Global stability of a lid-driven cavity with throughflow: flow visualisation studies. *Phys. Fluids* A **3**, 2081–2093.

Chapman, D. R. 1956 A theoretical analysis of heat transfer in regions of separated flow. *NACA TN* 3792.

Chapman, D. R., Kuehn, D. M. & Larson, H. K. 1958 Investigation of separated flows in supersonic and subsonic streams with emphasis on the effect of transition. *NACA Rep.* 1356.

Charwat, A. F. & Der, J. 1966 Studies on laminar and turbulent free shear layers with a finite initial boundary layer at separation. *AGARD CP* No. 4.

Chiang, T. P., Sheu, W. H. & Hwang, R. R. 1998 Effect of Reynolds number on the eddy structure in a lid-driven cavity. *Intl J. Numer. Meth. Fluids* **26**, 557–579.

Chung, P. M. & Viegas, J. R. 1961 Heat transfer at the reattachment zone of separated laminar boundary layers. *NASA TN* D-1072.

Cook, W. J. & Felderman, E. J. 1966 Reduction of data from thin-film heat-transfer gauges: a concise numerical technique. *AIAA J.* **4**, 561–562.

Denison, M. R. & Baum, E. 1963 Compressible free shear layer with finite initial thickness. *AIAA J.* **1**, 342–349.

Ding, Y. & Kawahara, M. 1998 Linear stability of incompressible fluid flow in a cavity using finite element method. *Intl J. Numer. Meth. Fluids* **27**, 139–157.

Dolling, D. S. & Murphy, M. T. 1983 Unsteadiness of the separation shock wave structure in a supersonic compression ramp flow. *AIAA J.* **21**, 1628–1634.

Erengil, M. E. & Dolling, D. S. 1991 Separation shock motion and ensemble-averaged wall pressures in a Mach 5 compression ramp interaction. *AIAA J.* **29**, 728–735.

Ghia, U., Ghia, K. N. & Shin, C. T. 1982 High-*Re* solutions for incompressible flow using the Navier–Stokes equations and a multigrid method *J. Comput. Phys.* **48**, 387–411.

Goldstein, S. 1930 Concerning some solutions of the boundary-layer equations in hydrodynamics. *Proc. Camb. Phil. Soc.* **26**, 18–30.

Hahn, M. 1969 Experimental investigation of separated flow over a cavity at hypersonic speed. *AIAA J.* **7**, 1092–1098.

Hillier, R., Kirk, D. & Soltani, S. 1995 Navier–Stokes computations of hypersonic flows. *Intl J. Numer. Meth. Heat Fluid Flow* **5**, 195–212.

Hodgson, J. W. 1970 Heat transfer in separated laminar hypersonic flow. *AIAA J.* **8**, 2291–2293.

Holden, M. 1971 Establishment time of laminar separated flows. *AIAA J.* **9**, 2296–2298.

Ihrig, H. K. & Korst, H. H. 1963 Quasi-steady aspects of the adjustment of separated flow regions to transient external flows. *AIAA J.* **1**, 934–937.

Keyes, F. G. 1952 The heat conductivity, viscosity, specific heat and Prandtl numbers for thirteen gases. *Project Squid TR* 37. M.I.T.

Kim, J. & Moin, P. 1985 Application of a fractional-step method to incompressible Navier–Stokes equations. *J. Comput. Phys.* **59**, 308–323.

Koseff, J. R. & Street, R. L. 1984 On end wall effects in a lid-driven cavity flow. *Trans. ASME: J. Fluids Engng* **106**, 385–389.

Kubota, T. & Dewey, C. F. 1964 Momentum integral methods for the laminar free shear layer. *AIAA J.* **2**, 625–629.

Larson, H. K. & Keating, S. J. 1960 Transition Reynolds numbers of separated flows at supersonic speeds. *NASA TN* D-349.

Mallinson, S. G., Gai, S. L. & Mudford, N. R. 1997*a* Establishment of steady separated flow over a compression-corner in a free piston shock tunnel. *Shock Waves* **7**, 249–253.

Mallinson, S. G., Hillier, R., Zanchetta, M. A., Soltani, S. & Kirk, D. 1997*b* An experimental and numerical study of hypersonic turbulent boundary layer flows. *AIAA Paper* 97-2290.

Merzkirch, W., Page, R. H. & Fletcher, L. S. 1988 A survey of heat transfer in compressible separated and reattached flows *AIAA J.* **26**, 144–150.

Morgenstern, A. & Chokani, N. 1994 Hypersonic flow past open cavities *AIAA J.* **32**, 2387–2393.

Nestler, D. E. 1970 A model of steady separated flow in cavities in hypersonic low density flow. *Proc. Third Intl Heat Transfer Conf.*, vol. 2., pp. 251–261. ASM

Nicoll, K. M. 1964 A study of laminar hypersonic cavity flows. *AIAA J.* **2**, 1535–1541.

Ramanan, N. & Homsy, G. M. 1994 Linear stability of lid-driven cavity flow. *Phys. Fluids* **6**, 2690–2701.

Rockwell, D. & Naudascher, E. 1978 Review – self-sustaining oscillations of flow past cavities. *Trans. ASME: J. Fluids Engng* **100**, 152–165.

Rom, J. 1963 Measurements of heat transfer in separated regions in a shock tube and in a shock tunnel. *AIAA J.* **1**, 2193–2194.

Roshko, A. & Thomke, G. J. 1966 Observation of turbulent reattachment behind an axisymmetric downstream-facing step in supersonic flow. *AIAA J.* **4**, 975–980.

Rossiter, J. E. 1966 Wind tunnel experiments on the flow over rectangular cavities at subsonic and transonic speeds. *Aero. Res. Coun. R & M* 3438.

Schultz, D. L. & Jones, T. V. 1973 Heat-transfer measurements in short-duration hypersonic facilities. *AGARDograph* 165.

Unalmis, O. H., Clemens, N. T. & Dolling, D. S. 1998 Planar laser imaging of high speed cavity flow dynamics. *AIAA Paper* 98-0776.

Zhang, X. 1995 Compressible cavity flow oscillation due to shear layer instabilities and pressure feedback. *AIAA J.* **33**, 1404–1411.